

Hyperspectral Image Super-Resolution via Deep Prior Regularization with Parameter Estimation

Xiuheng Wang, *Student Member, IEEE*, Jie Chen, *Senior Member, IEEE*, Qi Wei, *Member, IEEE*, and Cédric Richard, *Senior Member, IEEE*,

Abstract—Hyperspectral image (HSI) super-resolution is commonly used to overcome the hardware limitations of existing hyperspectral imaging systems on spatial resolution. It fuses a low-resolution (LR) HSI and a high-resolution (HR) conventional image of the same scene to obtain an HR HSI. In this work, we propose a method that integrates the physical model and deep prior information. A novel, yet effective two-stream fusion network is designed and its output serves as a regularization term of the fusion problem. Then, we optimize the fusion problem by solving a Sylvester equation, and simultaneously estimate the regularization parameter to automatically adjust contribution of the physical model and learnt prior to reconstruct the final HR HSI. Experimental results on two public datasets demonstrate the superiority of the proposed method over several state-of-the-art methods on both quantitative and qualitative comparisons.

Index Terms—HSI super-resolution, deep learning, fusion, Sylvester equation, regularization parameter estimation.

I. INTRODUCTION

HYPERSPECTRAL imaging simultaneously captures images of the same scene at different wavelengths. Rich spectral characteristics provided by hyperspectral images are important in remote sensing [1]. HSIs have been demonstrated to improve the performance of tasks including tracking [2], segmentation [3], classification [4]. HSIs contain richer spectral information of real scenes compared with conventional images such as color and gray-scale images. However, the high spectral resolution of hyperspectral images need to make a compromise with spatial resolution to ensure an acceptable signal-to-noise ratio (SNR) [5]. This in turn restricts applications of HSIs. To cope with this issue, a critical task is thus to improve the spatial resolution of HSIs.

Due to various physical limitations at hardware level, it is often challenging to develop hyperspectral cameras that simultaneously achieve high spatial and high spectral resolutions. On the other hand, conventional cameras capture RGB or panchromatic images with higher spatial resolution but lower spectral resolution by integrating the scene response over broad spectral bands [5]. Consequently, researchers have

proposed computational methods to restore a high-resolution (HR) HSI by integrating a low-resolution (LR) HSI and an HR conventional image [6], [7]. This procedure is often referred to as *HSI super-resolution* or *HSI fusion*. A class of fusion approaches is based on component substitution such as the intensity, hue and saturation (IHS) technique [8], principal component analysis (PCA) [9] and wavelet transform [10], [11]. These methods are fast but tend to introduce spectral distortion when estimating the scene response of the latent HR HSIs from panchromatic images.

Many researchers formulate the fusion problem as an image restoration optimization problem. In such approaches, following a physical degradation model, the input LR HSI and HR conventional images are seen as the spatially and spectrally degraded observations (i.e. linear down-sampled versions) of the latent HR HSI respectively. Note that the HSI super-resolution is a highly ill-posed problem owing to the large scaling factors in both spatial and spectral domain, thus, it is important to incorporate prior information from the latent HR HSI to constrain the solution space. Depending on the structures of prior information used in the optimization problem, existing techniques can be roughly divided into two categories as stated in [12]: spectral unmixing based approaches [5], [13], [14] and sparse representation based approaches [15]–[18].

It turns out that using priors for spectral unmixing with some constraints (e.g., non-negativity, sum-to-one) is beneficial for HSI super-resolution. In [13], the coupled nonnegative matrix factorization (CNMF) method is proposed to alternatively unmixing a LR HSI and a HR conventional image to estimate a HR HSI. In [5], with a similar framework, by jointly unmixing two input images, the initial optimization problem is first decoupled into two constrained least-square problems and then solved. The method proposed in [14] reconstructs the latent HR HSI with respect to its endmembers and their abundances by using the alternating direction method of multipliers (ADMM) technique [19]. Sparse representation is another promising technique for fusing hyperspectral and conventional images, aiming to sparsely encode the latent HR HSI with an appropriate spectral dictionary learnt from the input HSI. To this end, in [15] the spectral dictionary is learnt with K-SVD and sparse matrix factorization is used to fuse two input images. Considering the similarity of neighboring pixels in the latent HSI, the method proposed in [16] enforces group sparsity as well as non-negativity among pixels within small patches. The work [17] fuses the hyperspectral and conventional images in a variational approach and designs a sparse regularizer by decomposing the scene on a spectral

X. Wang and J. Chen are with with Centre of Intelligent Acoustics and Immersive Communications at School of Marine Science and Technology, Northwestern Polytechnical University, Xi'an, and also with China Key Laboratory of Ocean Acoustics and Sensing, Ministry of Industry and Information Technology, Xian 710072, China (e-mail: xiuheng.wang@mail.nwpu.edu.cn; dr.jie.chen@ieee.org).

Q. Wei is with University of Toulouse, IRIT/INP-ENSEEIH, 2 rue Camichel, BP 7122, 31071 Toulouse cedex 7, France. (e-mail: bjweiqi@gmail.com).

C. Richard is with Université Côte d'Azur, OCA, CNRS, 75016 Paris, France (cedric.richard@unice.fr).

dictionary. The method of [18] develops a non-negative sparse coding algorithm that exploits not only the sparsity of each pixel but also the non-local spatial similarity of the latent HR HSI, leading to enhanced fusion performance. However, these predefined priors-based methods with handcrafted regularizers have some inherent disadvantages. For example, a complex regularizer may introduce extra difficulties in solving the related optimization problem.

Recently, inspired by the successful application of deep learning to many computer vision tasks, especially single image super-resolution (SISR) [20], convolutional neural networks (CNNs) have been introduced to address the HSI super-resolution problem [21]–[26]. Compared to optimization methods based on predefined priors, these deep learning methods require fewer assumptions on the prior knowledge of the latent HR HSI, and can directly learn the relevant information from training data. However, these learning based methods sometimes ignore the blurring and down-sampling operators as well as the spectral response function in the degradation model, though this model has a clear physical interpretation that relates the LR HSI and the HR conventional image to the HR HSI.

In order to leverage the advantages of both optimization and deep learning methods, several deep priors-based approaches (i.e., learning the priors via deep CNNs) have been recently proposed [27], [28]. In these methods, deep neural networks are designed to exploit both spatial and spectral characteristics of the latent HR HSI, and their outputs then serve as regularizers. This allows these approaches to achieve enhanced performance. However, they learn deep priors from the images produced by solving a Sylvester equation [29] rather than two observed images. Thus, the efficacy of deep priors relies on the accuracy of the produced images in their HSI super-resolution schemes.

Although numerous works have explored the prior structures of the latent HR HSI, few of them have investigated the way of balancing the contribution of the physical model and learnt information in their frameworks. That is however a key point for the effective implementation of such methods. Since properly adjusting the regularization parameter is one useful way to balance the modeling error and regularization strength. A classical method for estimating regularization parameters is the generalized cross-validation (GCV) [30], which has been applied for image restoration in [31]. In [32], the regularization parameter is chosen by finding a point near the “corner” of the L-curve, which is formed by plotting the data fidelity term and the regularizer in log-log scale. However, the use of the log-log scale leads to a convexity loss of the L-curve [33]. Recently, basis pursuit has been formulated as a constrained least-square problem, and the corresponding Pareto front [34] has been proved convex and continuously differentiable over all points of interest in [35]. Inspired by this method, the work [36] proposes the maximum curvature criterion (MCC) and the minimum distance criterion (MDC) on the response surface (i.e., the linear plot of the data fidelity and regularization costs) and confirms their good performance in estimating the regularization parameter for non-negative HSI deconvolution.

Here, we aim at performing hyperspectral super-resolution

by combining the physical model-based optimization and deep learning for constructing data-driven priors. Before proceeding with the algorithm, we raise the following three critical points to guide the problem formulation and solving:

- How to design a proper deep neural network capable of learning prior information from multi-source data?
- How to derive a formulation that combine s the model-based problem and the learnt prior?
- How to balance the contribution of the physical model and prior learnt from data?

In this work, a new deep priors-based method is proposed to practically address the three issues pointed above. To avoid handcrafting regularizers as in existing predefined priors-based methods, we train a new effective two-stream fusion network (TSFN) to directly learn deep priors through the fusion of two input observed images rather than produced images. In order to integrate deep priors into the degradation model, the network output, which correspond to the extracted deep priors, is plugged into a regularization term of a convex bi-objective optimization problem based on the degradation model. For adjusting the contribution of the deep priors in the hyperspectral super-resolution problem, we adopt the MDC to the response curve of the bi-objective optimization problem for automatic selection of the regularization parameter with a golden-section search strategy. To the our best knowledge, this is the first work that is designed to balance deep learning approach and optimization approach in this mathematical way. Our experimental results show the effectiveness of the proposed HSI super-resolution strategy, offering improvement over the results of the state-of-the-art methods.

The rest of this paper is organized as follows. We formulate the HSI super-resolution problem in Section II. In Section III, the proposed method for HSI super-resolution is introduced. Section IV presents and discusses experimental results on two public datasets. Finally, conclusions and future works are given in Section V.

II. PROBLEM FORMULATION

Consider to reconstruct a high-resolution HSI $X_{3D} \in \mathbb{R}^{B \times L \times W}$ based on a low-resolution HSI $Y_{3D} \in \mathbb{R}^{B \times l \times w}$ and a high-resolution conventional image $Z_{3D} \in \mathbb{R}^{b \times L \times W}$ over the same scenario, where B and b are numbers of spectral bands of the hyperspectral and conventional images ($B > b$); (L, W) and (l, w) are the numbers of (rows, columns) of the HR and LR images respectively ($L > l, W > w$). For ease of mathematical formulation, X_{3D} , Y_{3D} and Z_{3D} are transformed in matrix forms $\mathbf{X} \in \mathbb{R}^{B \times N}$, $\mathbf{Y} \in \mathbb{R}^{B \times n}$ and $\mathbf{Z} \in \mathbb{R}^{b \times N}$, respectively, where $N = L \times W$, $n = l \times w$ are numbers of pixels in each band of the HR and LR images. According to the linear degradation model, \mathbf{Y} can be viewed as a spatially down-sampled vision of \mathbf{X} , while \mathbf{Z} is a down-sampled observation of \mathbf{X} in the spectral domain, so that:

$$\mathbf{Y} = \mathbf{XBS}, \quad \mathbf{Z} = \mathbf{RX}, \quad (1)$$

where $\mathbf{B} \in \mathbb{R}^{N \times N}$ represents the blurring matrix, $\mathbf{S} \in \mathbb{R}^{N \times n}$ is a uniform down-sampling operator with scaling factor $s = N/n$ and $\mathbf{R} \in \mathbb{R}^{b \times B}$ denotes the spectral response function

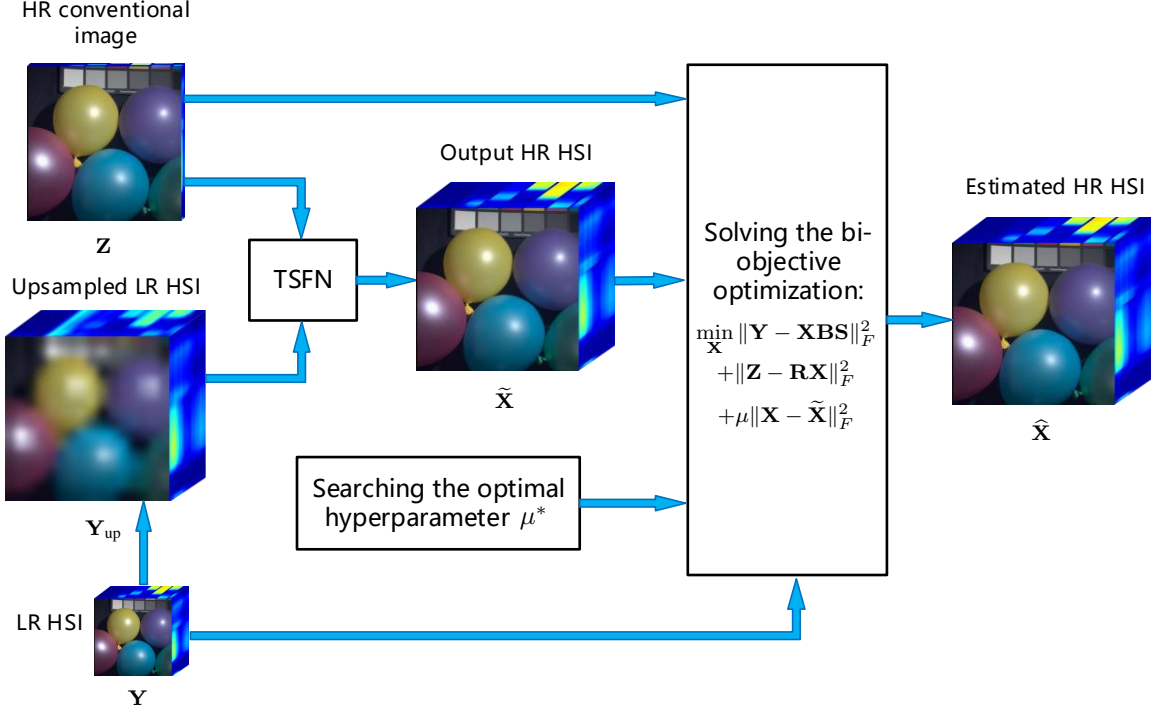


Fig. 1. Overall scheme of our proposed HSI super-resolution method. HR and LR represent high-resolution and low-resolution in spatial domains, respectively.

(SRF) of the conventional camera sensor, which is often known or can be estimated a priori. Moreover, the blurring matrix \mathbf{B} is assumed to be a known block circulant matrix with circulant blocks [17]. In this widely admitted assumption, \mathbf{B} can be decomposed as $\mathbf{B} = \mathbf{F}\mathbf{D}\mathbf{F}^H$. Here, $\mathbf{F} \in \mathbb{R}^{N \times N}$ is the discrete Fourier transform (DFT) matrix ($\mathbf{F}\mathbf{F}^H = \mathbf{I}_N$, where \mathbf{I}_N is an $N \times N$ identity matrix.) and $\mathbf{D} \in \mathbb{R}^{N \times N}$ is a diagonal matrix containing the eigenvalues of \mathbf{B} .

Based on the degradation model in (1), we can estimate \mathbf{X} by introducing proper priors and seeking the minimum of the following bi-objective function:

$$\begin{aligned} \hat{\mathbf{X}} &= \arg \min_{\mathbf{X}} \mathcal{J}(\mathbf{X}) \\ &= \arg \min_{\mathbf{X}} \mathcal{J}_1(\mathbf{X}) + \mu \mathcal{J}_2(\mathbf{X}) \end{aligned} \quad (2)$$

where

$$\mathcal{J}_1(\mathbf{X}) = \|\mathbf{Y} - \mathbf{XBS}\|_F^2 + \|\mathbf{Z} - \mathbf{RX}\|_F^2 \quad (3)$$

with $\|\cdot\|_F$ denoting the matrix Frobenius norm. $\mathcal{J}_1(\mathbf{X})$ is the data fidelity terms and $\mathcal{J}_2(\mathbf{X})$ is a regularizer that enforces the desired property of the solution while $\mu \geq 0$ is the hyperparameter to balance the data fidelity term \mathcal{J}_1 and the regularization term \mathcal{J}_2 . As shown in (2), prior information on the latent HR HSI is encoded in $\mathcal{J}_2(\mathbf{X})$. Handcrafting a powerful regularizer $\mathcal{J}_2(\mathbf{X})$ is non-trivial. Recently, benefitting from the variable splitting techniques, plug-and-play methods have been proposed to solve various hyperspectral image inverse problems [37]–[39]. On the contrary, in this work, we construct a regularizer leveraging the network output $\tilde{\mathbf{X}} \in \mathbb{R}^{B \times N}$ to enforce the solution of (3) to be close to the learnt deep priors. More specifically, let $\mathcal{J}_2(\mathbf{X})$ be the squared Euclidean distance

between \mathbf{X} and $\tilde{\mathbf{X}}$:

$$\mathcal{J}_2(\mathbf{X}) = \|\mathbf{X} - \tilde{\mathbf{X}}\|_F^2 \quad (4)$$

Then (2) is given by

$$\arg \min_{\mathbf{X}} \|\mathbf{Y} - \mathbf{XBS}\|_F^2 + \|\mathbf{Z} - \mathbf{RX}\|_F^2 + \mu \|\mathbf{X} - \tilde{\mathbf{X}}\|_F^2 \quad (5)$$

Compared to other possible formulations, (5) allows simple and fast resolving steps. Using a powerful priors structure for $\tilde{\mathbf{X}}$, appropriately integrating the priors into the degradation model as well as balancing contribution of the priors are three key points to obtain a good estimation of the latent HR HSI.

III. PROPOSED METHOD

In this section, we present the proposed deep priors-based HSI super-resolution approach in detail. Firstly, we introduce the architecture design of the two-stream fusion network. Then, we invoke an efficient approach for solving the bi-objective optimization problem in (5) based on a Sylvester analytical solver. Finally, we balance the contribution of the learnt deep priors by seeking the optimal value of hyperparameter μ^* under the maximum curvature criterion. The overall scheme of our method is illustrated in Fig. 1.

A. Deep Priors Learning and Network Design

Instead of using handcrafted regularizers, we propose to learn the priors of the latent HR HSI from hyperspectral datasets by carefully designing a deep CNN with the two-stream architecture, i.e., TSFN. Note that the deep priors learning process is performed in the 3D image domain.

In contrast to the single-stream architecture used in [27], [28], the two-stream deep neural networks extract and combine

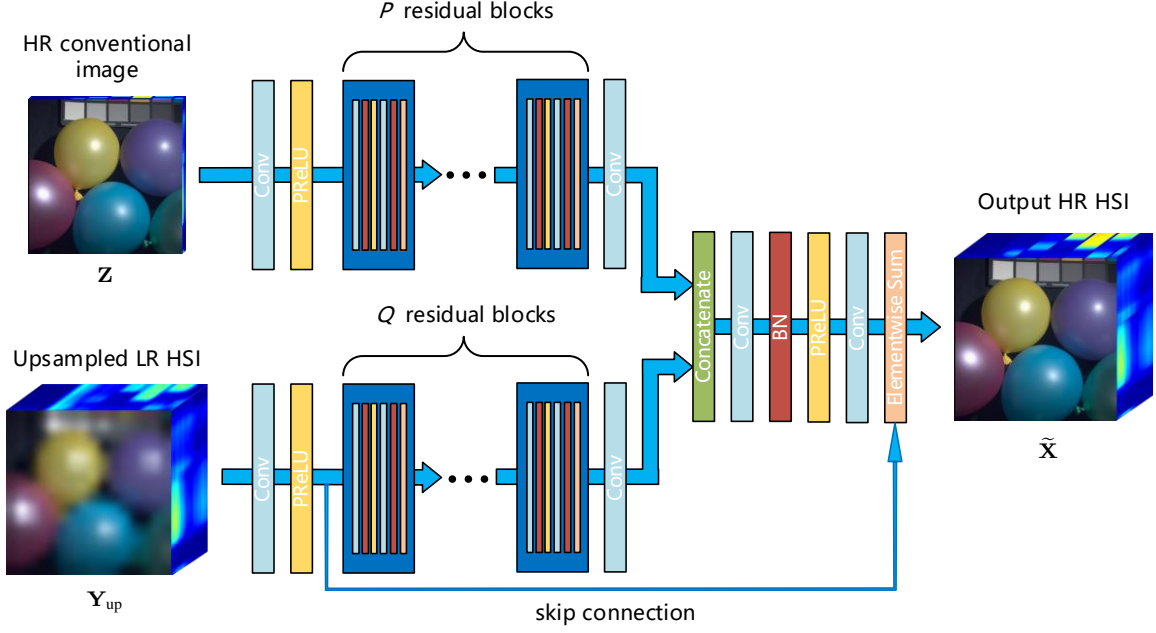


Fig. 2. Two-stream architecture for hyperspectral image super-resolution.

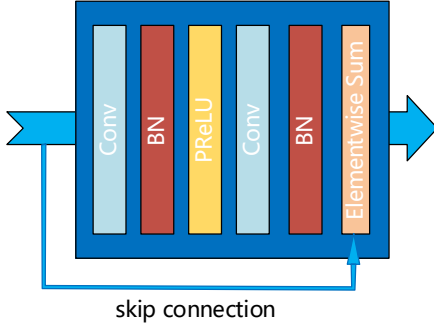


Fig. 3. Detail components of the residual block.

features of bimodal data to fuse information at the feature level, which has been proved to be a powerful tool in applications including videos action recognition [40], [41], hyperspectral classification [42] and hyperspectral superresolution [24]–[26]. In this work, we design a deep network architecture by employing the residual blocks [43] and a skip-connection [44]. These techniques have been shown useful in boosting the performance in SISR approaches [45], [46].

As illustrated in Fig. 2, the proposed TSFN architecture takes an up-sampled image $\mathbf{Y}_{up} \in \mathbb{R}^{B \times N}$ (produced from an LR HSI \mathbf{Y} via the bicubic interpolation) and a HR conventional image \mathbf{Z} as two inputs. In order to achieve a robust HR HSI estimation $\tilde{\mathbf{X}}$, the spatial context in \mathbf{Z} and spectral attribute in \mathbf{Y} are simultaneously learnt. The feature maps of \mathbf{Z} and \mathbf{Y} extracted by the two corresponding streams, containing P and Q residual blocks respectively, are concatenated. Then, the concatenated information is fed into the next convolutional layer. The core of our network is the residual block, containing two convolutional (Conv) layers followed by batch-normalization (BN) layers [47] and

ParametricReLU (PReLU) [48] as the activation function (see Fig. 3). The batch-normalization layer is used to speed up the training process as well as boost the image restoration performance. The skip connection path passes input feature maps to the output of the residual block via element-wise sum. A skip connection operator is also employed to add the shallowest feature maps extracted from \mathbf{Y}_{up} to the deepest feature maps of the network to reconstruct the final $\tilde{\mathbf{X}}$. The last convolutional layer contains B filters while the others are composed of 64 filters, and the kernel size of each filter is 3×3 with a stride of 1. The matrix ℓ_1 -norm based loss function is used:

$$\ell(\Theta) = \sum_{m=1}^M \|\mathcal{F}(\mathbf{Y}_{up,m}, \mathbf{Z}_m; \Theta) - \mathbf{X}_m\|_1 \quad (6)$$

where $\{(\mathbf{Y}_{up,m}, \mathbf{Z}_m; \mathbf{X}_m)\}_{m=1}^M$ represent M training image (patch) pairs used to train the network function \mathcal{F} parameterized by Θ . Note that ℓ_1 -norm is used since we found it leads to better performance than ℓ_2 -norm by trial and error.

It is worth noting that the proposed TSFN can be applied to effectively learn priors of the latent HR HSI in degraded scenarios with various scaling factor settings (e.g., 8, 16 and 32). Our network architecture bears some resemblance to that in [26]. The main difference is that [26] uses the attention residual block while our model extracts the feature through the residual block without the attention mechanism. Further, we avoid adopting the deconvolution layer and train our model with a mixture of image pairs with different scaling factors. In this way, our trained model can flexibly handle different scenarios.

B. Integrating Deep Priors into the Degradation Model

The fusion result inferred from the proposed TSFN, referred to $\tilde{\mathbf{X}}$, is used in the regularizer \mathcal{J}_2 . More specifically, $\tilde{\mathbf{X}}$,

Algorithm 1 Solution by solving the Sylvester Equation w.r.t. $\tilde{\mathbf{X}}$.

Input: $\mathbf{Y}, \mathbf{Z}, \mathbf{B}, \mathbf{S}, \mathbf{R}, \tilde{\mathbf{X}}, \mu$.

Output: $\hat{\mathbf{X}}$.

Initialize $\mathbf{C}_1 = \mathbf{R}^T \mathbf{R} + \mu \mathbf{I}_B$,

$\mathbf{C}_2 = (\mathbf{BS})(\mathbf{BS})^T$,

$\mathbf{C}_3 = \mathbf{R}^T \mathbf{Z} + \mathbf{Y}(\mathbf{BS})^T + \mu \tilde{\mathbf{X}}$.

(a) Eigen-decomposition of \mathbf{B} :

$$\mathbf{B} = \mathbf{F} \mathbf{D} \mathbf{F}^H$$

(b) $\bar{\mathbf{D}} = \mathbf{D}(\mathbf{1}_s \otimes \mathbf{I}_n)$

(c) Eigen-decomposition of \mathbf{C}_1 :

$$\mathbf{C}_1 = \mathbf{Q} \mathbf{\Lambda} \mathbf{Q}^{-1}$$

(d) $\bar{\mathbf{C}}_3 = \mathbf{Q}^{-1} \mathbf{C}_3 \mathbf{F}$

(e) Compute auxiliary matrix $\bar{\mathbf{X}}$ band by band

for $k = 1$ to B **do**

$$\bar{\mathbf{X}}_k = \lambda_k^{-1} (\bar{\mathbf{C}}_3)_k - \lambda_k^{-1} (\bar{\mathbf{C}}_3)_k \bar{\mathbf{D}} (\lambda_k s \mathbf{I}_n + \sum_{t=1}^s \mathbf{D}_t^2) \bar{\mathbf{D}}^H$$

end for

(f) $\hat{\mathbf{X}} = \mathbf{Q} \bar{\mathbf{X}} \mathbf{F}^H$

a representation of the prior spatial-spectral information of the latent \mathbf{X} , is used to regularize the final estimation $\hat{\mathbf{X}}$, as illustrated in the bi-objective optimization problem (5). To solve (5), we force the derivative of the loss function w.r.t. \mathbf{X} to be zero. Thus, the optimum of (5) is defined by the solution of following Sylvester equation:

$$\mathbf{C}_1 \hat{\mathbf{X}} + \hat{\mathbf{X}} \mathbf{C}_2 = \mathbf{C}_3 \quad (7)$$

where

$$\begin{aligned} \mathbf{C}_1 &= \mathbf{R}^T \mathbf{R} + \mu \mathbf{I}_B \\ \mathbf{C}_2 &= (\mathbf{BS})(\mathbf{BS})^T \\ \mathbf{C}_3 &= \mathbf{R}^T \mathbf{Z} + \mathbf{Y}(\mathbf{BS})^T + \mu \tilde{\mathbf{X}} \end{aligned} \quad (8)$$

where \mathbf{I}_B represents the identity matrix of size $B \times B$. According to the well-known conclusion in [29], the Sylvester equation in (7) has a unique solution if and only if an arbitrary sum of the eigenvalues of \mathbf{C}_1 and \mathbf{C}_2 is not equal to zero. $\mathbf{R}^T \mathbf{R}$ and \mathbf{I}_B are both positive-definite matrices, and thus, \mathbf{C}_1 is positive-definite. Further considering that \mathbf{C}_2 is positive semi-definite, an arbitrary sum of the eigenvalues of \mathbf{C}_1 and \mathbf{C}_2 is greater than zero, which ensures the uniqueness of the solution in (7). The fast algorithm for solving (7) can be achieved by referring to our previous work [49], with steps summarized in Algorithm 1.

C. Adjusting the Contribution from Deep Priors

Different from previous deep priors-based approaches [27], [28], achieving a good balance between the data fidelity and regularization terms is also considered in our work. Intuitively, if μ increases toward infinity, the regularization term $\|\mathbf{X} - \tilde{\mathbf{X}}\|_F^2$ will be minimized, i.e., the solution will be $\tilde{\mathbf{X}}$. On the contrary, the solution tends to minimize the data fidelity terms $\|\mathbf{Y} - \mathbf{XBS}\|_F^2 + \|\mathbf{Z} - \mathbf{RX}\|_F^2$ when the value of μ leads to zero. In this subsection, we propose to estimate the regularization parameter with the MDC that is initially used for hyperspectral image deconvolution [36]. We estimate

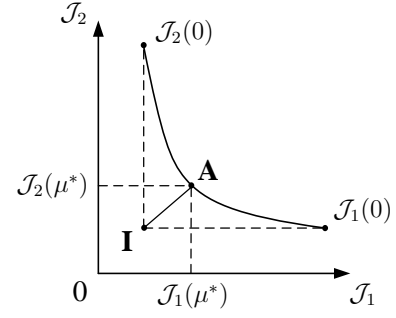


Fig. 4. Representation of the response curve. The optimal point is denoted as $\mathbf{A}(\mathcal{J}_1(\mu^*), \mathcal{J}_2(\mu^*))$.

the response curve of (5) that describes the characteristic of the solution set obtained by varying hyperparameter value μ . Then, MDC is adopted to the estimated response curve to seek the optimal value of μ in the hyperspectral super-resolution problem by using the golden-section search method.

Problem (5) can also be considered as a bi-objective optimization in form of

$$\hat{\mathbf{X}} = \arg \min_{\mathbf{X}} (\mathcal{J}_1(\mathbf{X}), \mathcal{J}_2(\mathbf{X})) \quad (9)$$

1) *Pareto Front*: The definition of Pareto front depends on the notion of *domination* defined in [34]. This notion is important in the bi-objective optimization since it gives a criterion of judging a better solution. Let $\hat{\mathbf{X}}^{(1)}$ and $\hat{\mathbf{X}}^{(2)}$ be two different solutions of the bi-objective optimization in (9). When we say $\hat{\mathbf{X}}^{(1)}$ dominates $\hat{\mathbf{X}}^{(2)}$, it means that $\mathcal{J}_i(\mathbf{X}^{(1)})$ is not larger than $\mathcal{J}_i(\mathbf{X}^{(2)})$ for all $i \in \{1, 2\}$ and $\mathcal{J}_j(\mathbf{X}^{(1)})$ is smaller than $\mathcal{J}_j(\mathbf{X}^{(2)})$ for at least one $j \in \{1, 2\}$:

$$\hat{\mathbf{X}}^{(1)} \preceq \hat{\mathbf{X}}^{(2)} \text{ iff } \begin{cases} \mathcal{J}_i(\mathbf{X}^{(1)}) \leq \mathcal{J}_i(\mathbf{X}^{(2)}), & \forall i \in \{1, 2\} \\ \exists i \in \{1, 2\} & \text{s.t. } \mathcal{J}_i(\mathbf{X}^{(1)}) < \mathcal{J}_i(\mathbf{X}^{(2)}) \end{cases} \quad (10)$$

Apart from that, the solution $\hat{\mathbf{X}}^{(1)}$ does not dominate $\hat{\mathbf{X}}^{(2)}$. The solution is said to be non-dominated or *Pareto optimal* for a bi-objective problem if all other solutions in the feasible region have higher values for at least one objective. The set containing all the non-dominated solutions is defined as the *Pareto front*. It means that any point in the Pareto front cannot be said to dominate any other. The shape of Pareto front denotes the set of all the achievable trade-offs between two objectives $\mathcal{J}_1(\mathbf{X})$ and $\mathcal{J}_2(\mathbf{X})$.

In our case, there is a trade-off between $\mathcal{J}_1(\mathbf{X})$ and $\mathcal{J}_2(\mathbf{X})$ controlled by the regularization parameter μ . By solving (5) via Algorithm 1, each value of μ yields a solution:

$$\hat{\mathbf{X}}_\mu = \arg \min_{\mathbf{X}} \mathcal{J}(\mathbf{X}) = \arg \min_{\mathbf{X}} \mathcal{J}_1(\mathbf{X}) + \mu \mathcal{J}_2(\mathbf{X}) \quad (11)$$

and a point $(\mathcal{J}_1(\hat{\mathbf{X}}_\mu), \mathcal{J}_2(\hat{\mathbf{X}}_\mu))$ of the response curve. According to the theorem in [36], this response curve is convex and exactly coincides with the Pareto front because $\mathcal{J}(\mathbf{X})$ is convex. For notation simplicity, we will write the point as $(\mathcal{J}_1(\mu), \mathcal{J}_2(\mu))$ and $\mathcal{J}(\hat{\mathbf{X}}_\mu)$ as $\mathcal{J}(\mu)$.

2) *Minimum Distance Criterion*: The minimum distance criterion [36] allows us to search the optimal point $\mathbf{A}(\mathcal{J}_1(\mu^*), \mathcal{J}_2(\mu^*))$ on the response curve with μ^* being the optimal

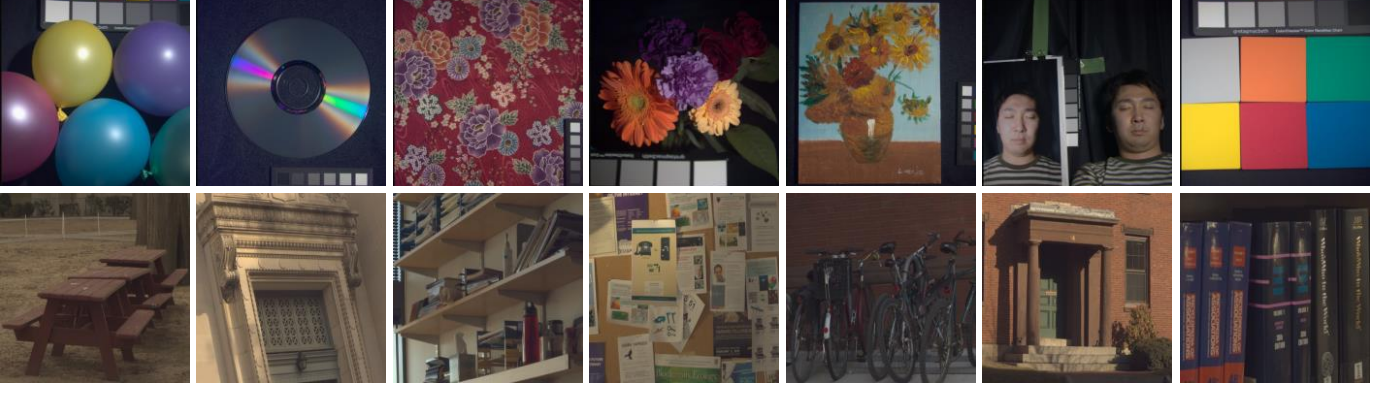


Fig. 5. Some color images from the CAVE dataset [50] (the first row) and the Harvard dataset [51] (the second row).

Algorithm 2 Deep Priors-Based HR Hyperspectral Image Super-Resolution.

Input: \mathbf{Y} , \mathbf{Z} , \mathbf{B} , \mathbf{S} , \mathbf{R} , Θ , α , a , b , δ , ϵ .

Output: $\hat{\mathbf{X}}$.

Initialize \mathbf{Y}_{up} from \mathbf{Y} with the bicubic interpolation.

(a) Obtain representation of learnt deep-priors via TSFN:

$$\hat{\mathbf{X}} = \mathcal{F}(\mathbf{Y}_{\text{up}}, \mathbf{Z}; \Theta)$$

(b) Search the optimal hyperparameter:

repeat

$$\mu_1 = a + \delta(b - a);$$

$$\mu_2 = b - \delta(b - a);$$

Compute $\hat{\mathbf{X}}_{\mu_1}$ and $\hat{\mathbf{X}}_{\mu_2}$ via (5) using Algorithm 1;

Obtain $\mathcal{D}(\mu_1)$ and $\mathcal{D}(\mu_2)$ via (13);

if $\mathcal{D}(\mu_1) < \mathcal{D}(\mu_2)$ **then**

$$b = \mu_2$$

else

$$a = \mu_1$$

end if

until $b - a < \epsilon$

(c) $\mu^* = \alpha(a + b)/2$;

(d) Output $\hat{\mathbf{X}} = \hat{\mathbf{X}}_{\mu^*}$ via (5) using Algorithm 1;

optimal hyperparameter is given by

$$\mu^* = \alpha \arg \min_{\mu} \mathcal{D}(\mu) \quad (14)$$

The varying range of μ is $(0, \infty)$. In practice, the value of μ cannot be set to ∞ but can be fixed to a large value b . Meanwhile, the lower bound of μ is set to a small value a rather than zero to avoid leading to highly ill-posed problems.

3) *Optimal Point Search:* The MDC is proved unimodal and always admits a unique minimum since the response curve is convex [36]. It is possible to design a fast approach aiming at finding the optimal point \mathbf{A} on the response curve. We propose to use the golden-section search method that is able to efficiently find the optimum point for the unimodal function [52]. This method operates in the interval $[a, b]$ and generates two intermediate points :

$$\begin{aligned} \mu_1 &= a + \delta(b - a) \\ \mu_2 &= b - \delta(b - a) \end{aligned} \quad (15)$$

where $\delta = 0.618$ is the golden ratio. The evaluated values of $\mathcal{D}(\mu_1)$ and $\mathcal{D}(\mu_2)$ are then compared and, if $\mathcal{D}(\mu_1) < \mathcal{D}(\mu_2)$, then μ_2 replaces b (else, μ_1 replaces a). This procedure is repeated in the new smaller interval $[a, b]$ until $b - a < \epsilon$ where $\epsilon > 0$ is an allowable final length of uncertainty. Finally, the estimated optimal hyperparameter is given by

$$\mu^* = \alpha(a + b)/2 \quad (16)$$

The proposed HSI super-resolution framework is summarized in Algorithm 2.

IV. EXPERIMENTS

In this section, several experiments are conducted to illustrate the effectiveness of our framework. The results provided by the proposed method are compared with those of state-of-the-art HSI super-resolution methods from both quantitative and qualitative perspectives.

A. Dataset and Experimental Setup

In this study, two public hyperspectral datasets, i.e., the CAVE dataset [50] and the Harvard dataset [51], are used to

parameter value. As represented in Fig. 4, this optimal point A is at minimum distance to the *ideal point* \mathbf{I} , which is defined as (I_1, I_2) and corresponds to the point whose coordinates are minimum in the two objectives:

$$\begin{aligned} I_1 &= \mathcal{J}(0) = \arg \min_{\mathbf{X}} \mathcal{J}_1(\mathbf{X}) \\ I_2 &= \mathcal{J}(\infty) = \arg \min_{\mathbf{X}} \mathcal{J}_2(\mathbf{X}) \end{aligned} \quad (12)$$

Unlike the HSI deconvolution problem in [36], the value of \mathcal{J}_1 is typically much smaller than \mathcal{J}_2 in the HSI super-resolution problem since \mathcal{J}_1 involves less pixels ($B \times n \times n$ and $b \times N \times N$) compared to \mathcal{J}_2 with $B \times N \times N$ pixels. Considering the large scale difference between \mathcal{J}_1 and \mathcal{J}_2 , we propose to use a scaled distance as

$$\mathcal{D}(\mu) = (\mathcal{J}_1(\mu) - I_1)^2 + \alpha(\mathcal{J}_2(\mu) - I_2)^2 \quad (13)$$

where $\alpha = (b/B)^2 + (1/s^2)^2$ is the scaling factor. Then the

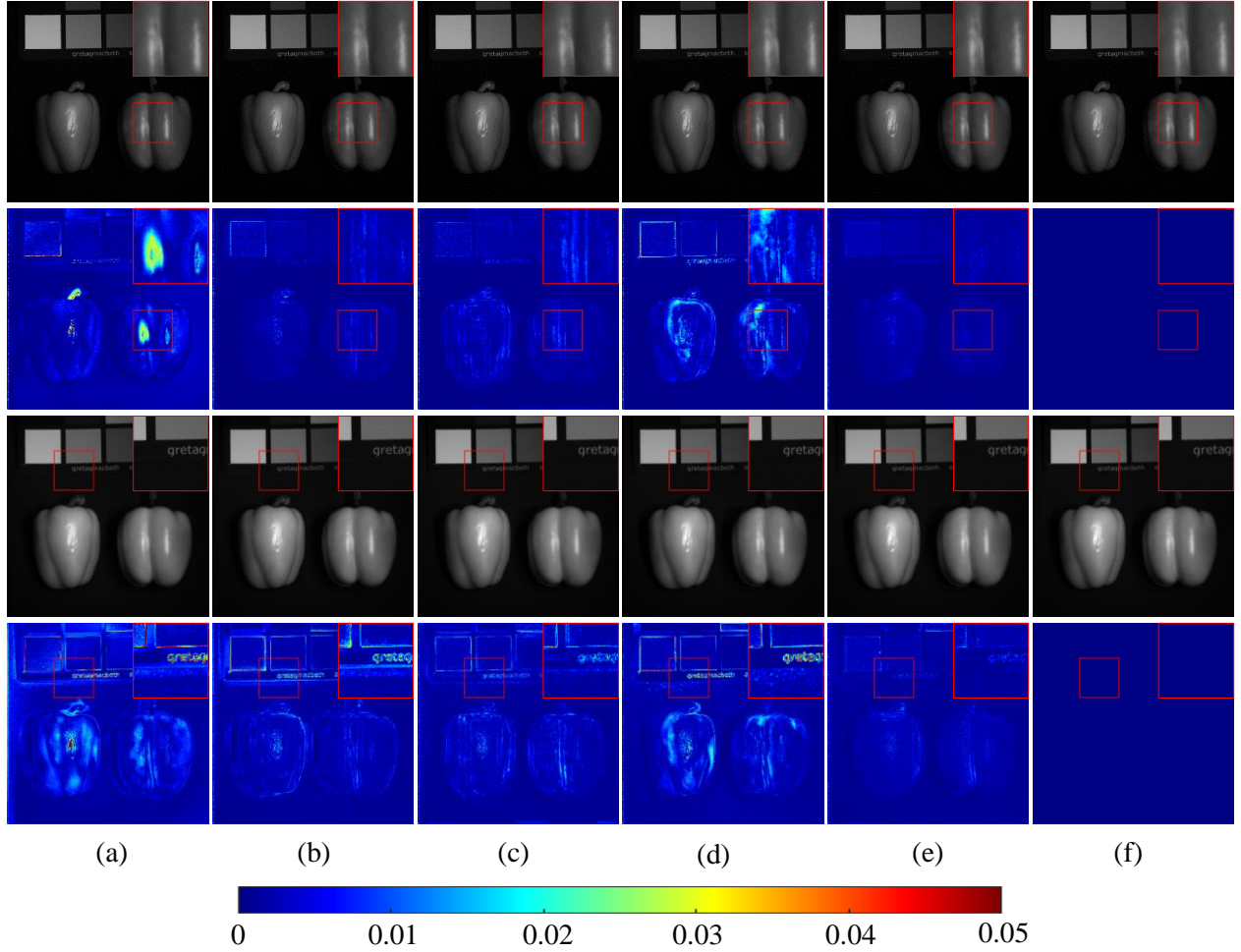


Fig. 6. Reconstructed images and corresponding error maps of the image *Real* and *fake peppers* from the CAVE dataset ($s = 16$) at 550 nm band (first and second rows) and 690 nm band (third and fourth rows). (a) CSU. (b) NSSR. (c) DHSIS. (d) CMS. (e) Proposed. (f) Ground Truth.

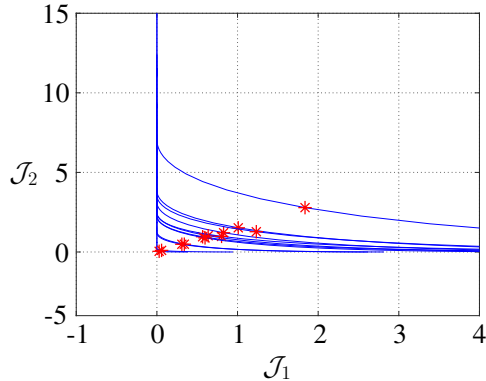


Fig. 7. Response curves (blue) and optimal points (red) with the scaling factor $s = 8$ on the CAVE dataset. Each curve corresponds to a test image.

evaluate the performance of our proposed method. The CAVE dataset consists of 32 indoor HSI recorded under controlled illuminations, each of which is of size 512×512 in spatial domain and contains 31 spectral bands ranging from 400 nm to 700 nm at a wavelength interval of 10 nm. In the Harvard dataset, there are 50 indoor and outdoor HSI captured under

daylight illumination. These images consist of 1392×1040 pixels, with 31 spectral bands of 10 nm, covering the visible spectrum 420 to 720 nm. The top left 1024×1024 pixels are cropped and extracted in our experiments. Examples of color images from these two datasets are shown in Fig. 5.

In our experiments, we follow the standard HSI super-resolution setups as in [18] and [12]. More specifically, the HSIs from two datasets are scaled into the range of $[0, 1]$, then serve as the ground truth of \mathbf{X} . The LR HSI \mathbf{Y} is generated by down-sampling the ground truth over disjointing $s \times s$ blocks, where scaling factor s is set to 8, 16 and 32 to demonstrate the good generalization of the proposed method. The HR conventional (RGB) image \mathbf{Z} is simulated by down-sampling the ground truth in the spectral domain using the spectral response function \mathbf{R} , which is derived from the response of a Nikon D700 camera¹. As in [27], we select the first 20 images from the CAVE dataset as the training set and the rest as the test set. In the Harvard dataset, the first 30 images are used for training while the others are used for testing. For the golden-section search method, we set $a = 10^{-8}$, $b = 1$ and $\epsilon = 0.01$.

¹<https://www.maxmax.com/faq/camera-tech/spectral-response/nikon-d700-study.htm>.

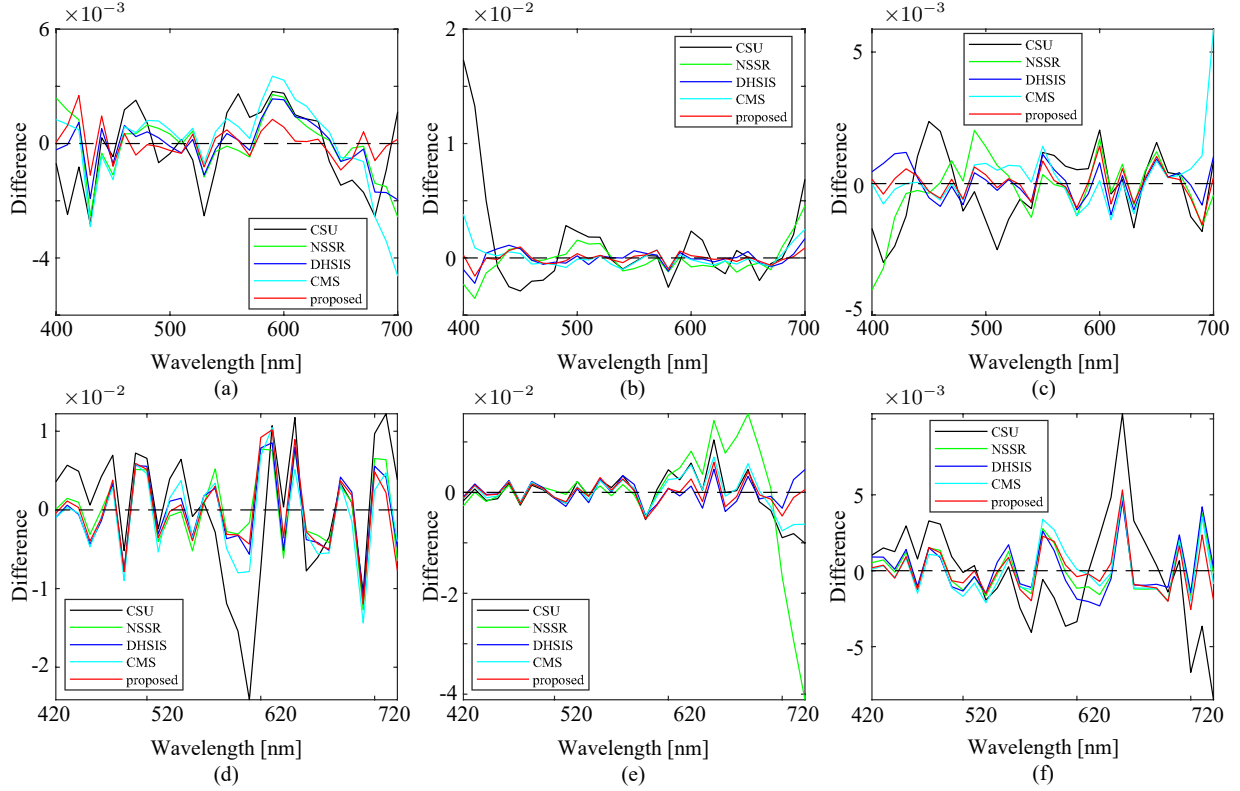


Fig. 8. Spectral differences with respect to the ground truths at three randomly selected locations. (a)-(c): image *Real and fake peppers* from the CAVE dataset. (d)-(f): image *img1* from the Harvard dataset when the scaling factor $s = 16$.

TABLE I
AVERAGE RMSE, PSNR, ERGAS, SAM OF DIFFERENT METHODS WITH THREE SCALING FACTORS ($s = 8, 16, 32$) ON THE CAVE DATASET.

	Metric	CSU	NSSR	DHSIS	CMS	proposed
$s = 8$	RMSE	2.57 ± 0.97	1.47 ± 0.53	1.36 ± 0.47	1.65 ± 0.59	1.15 ± 0.39
	PSNR	41.76 ± 3.47	$46.66 \pm \mathbf{2.91}$	47.01 ± 3.27	45.29 ± 2.97	48.44 ± 3.16
	ERGAS	1.196 ± 0.672	0.665 ± 0.315	0.621 ± 0.365	0.734 ± 0.339	0.522 ± 0.302
	SAM	6.27 ± 3.01	3.72 ± 1.46	3.74 ± 1.69	3.89 ± 1.46	3.52 ± 1.39
$s = 16$	RMSE	2.82 ± 0.95	1.77 ± 0.64	1.79 ± 0.64	1.99 ± 0.68	1.43 ± 0.51
	PSNR	41.01 ± 3.27	45.31 ± 3.11	44.74 ± 3.60	$43.94 \pm \mathbf{3.06}$	46.77 ± 3.52
	ERGAS	0.643 ± 0.333	0.398 ± 0.196	0.391 ± 0.199	0.445 ± 0.231	0.319 ± 0.184
	SAM	6.47 ± 3.02	4.32 ± 1.66	4.57 ± 1.88	4.37 ± 1.61	3.78 ± 1.56
$s = 32$	RMSE	3.02 ± 1.09	2.24 ± 0.84	2.45 ± 0.98	2.35 ± 0.80	1.83 ± 0.72
	PSNR	40.44 ± 3.49	43.49 ± 3.19	42.34 ± 4.03	$42.66 \pm \mathbf{3.03}$	44.88 ± 3.92
	ERGAS	0.336 ± 0.170	0.244 ± 0.109	0.257 ± 0.117	0.257 ± 0.117	0.196 ± 0.099
	SAM	6.83 ± 3.01	5.22 ± 1.98	5.87 ± 2.30	$5.04 \pm \mathbf{1.85}$	4.59 ± 1.86

B. Network Implementation Details

We implement the proposed two-stream fusion network using PyTorch framework and initialize the model using the method *HeUniform* [48]. The Adam optimizer [53] is utilized to minimize the loss function in (6) with an initial learning rate 0.0002 and a mini-batch of 16 in 500 epochs. In the training phase, each original HR HSI is cropped into 100 patches of size 256×256 , and each patch is randomly flipped and rotated for data augmentation before randomly generating an LR HSI and an HR conventional image in different degraded scenarios. When testing, we remove batch-normalization [47]. Each

stream contains 12 identical residual blocks ($P, Q = 12$) in our model. Note that the proposed two-stream fusion network is actually trained separately in two datasets.

C. Compared Methods and Quantitative Metrics

We have compared the results of our method with four state-of-the-art HSI super-resolution methods: Coupled Spectral Unmixing (CSU) method [5], Non-negative Structured Sparse Representation (NSSR) method [18], Clustering Manifold Structure (CMS) method [12] and Deep Hyperspectral Image Sharpening (DHSIS) method [27]. CSU aims to regularize

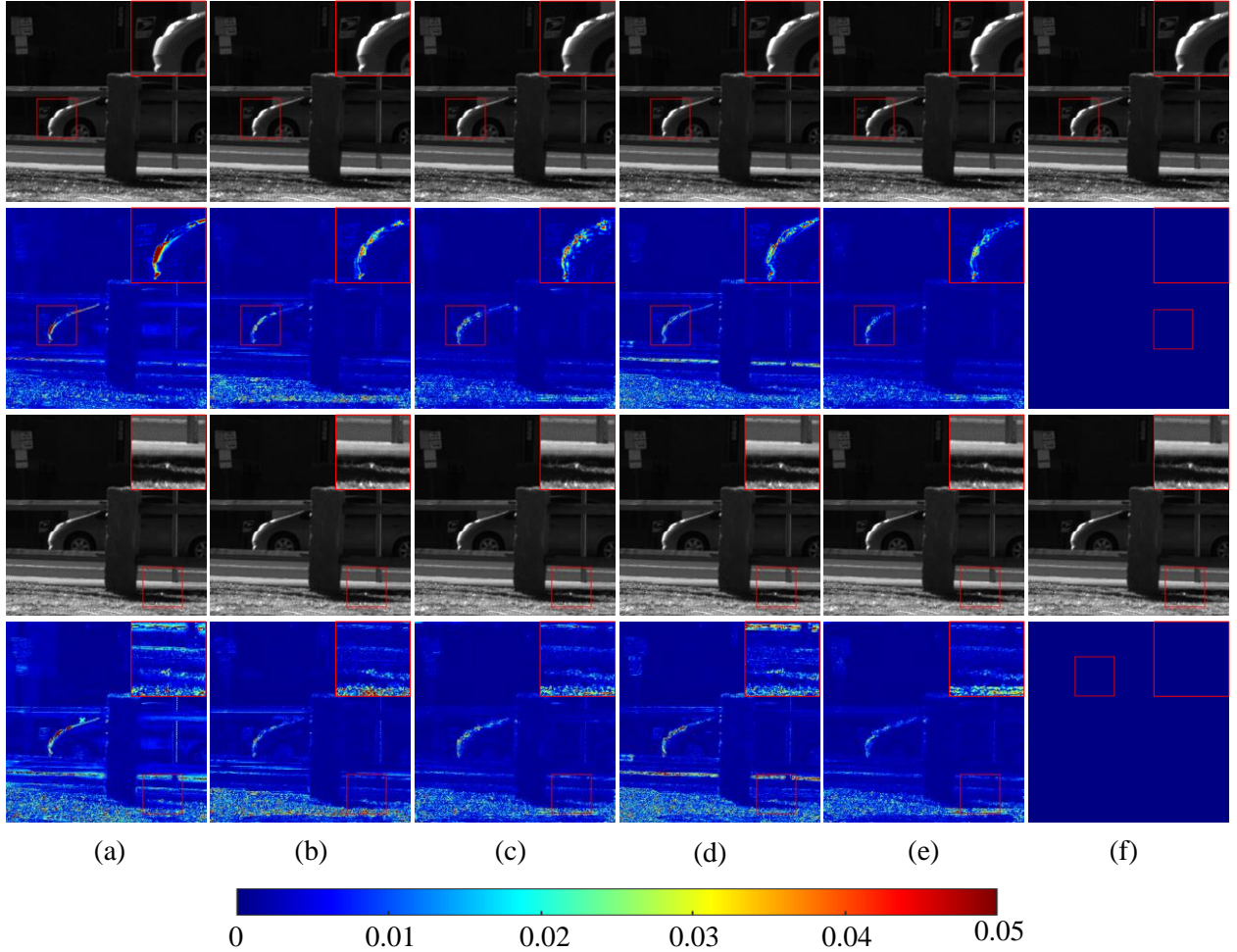


Fig. 9. Reconstructed images and corresponding error maps of the image *imgf1* from the Harvard dataset ($s = 16$) at 650 nm band (first and second rows) and 700 nm band (third and fourth rows). Columns: (a) CSU. (b) NSSR. (c) DHSIS. (d) CMS. (e) Proposed. (f) Ground Truth.

the HSI super-resolution problem by considering the spectral unmixing constraints. NSSR focuses on the sparse representation of the latent HR HSI as the prior structure for super-resolution. CMS exploits the manifold structure to capture the spatial correlation of the latent HR HSI to constrain the super-resolution scheme. In DHSIS, the priors of latent HR HSI are learnt by a deep neural network using massive data pairs without the use of pre-trained models. All these methods are implemented with their published codes online with default parameter settings. Note that we separately train the deep neural network for different scaling factors, blurring kernels and datasets in DHSIS. To evaluate the quality of reconstructed hyperspectral images, four quantitative metrics including the root-mean-square error (RMSE), the peak-signal-to-noise-ratio (PSNR), the erreur relative globale adimensionnelle de synthèse (ERGAS) [54] and the spectral angle mapper (SAM) [55] have been used in our study.

D. Performance Evaluation

We validate the proposed method to show its effectiveness in terms of super-resolution performance over other compared methods on the two datasets.

1) *Evaluation on CAVE Dataset:* Firstly, we conduct and compare all methods to restore each latent HR HSI \mathbf{X} from the corresponding LR HSI \mathbf{Y} and HR conventional image \mathbf{Z} with scale factor s in the CAVE dataset. The average values and standard deviations of RMSE, PSNR, ERGAS and SAM of the compared methods with different scaling factors on the CAVE dataset are reported in Table I. It is clear that the proposed method outperforms all competing methods for all different settings. Especially when the scaling factor is small (e.g., $s = 8$), the superiority and robustness of our method are more significant. The improvement mainly stems from the effectiveness of the learnt priors considering both spatial context and spectral attributes of the latent HR HSIs. Furthermore, the regularization parameter estimation also contributes to the satisfactory performance by giving a good trade-off between the data fidelity and regularization terms. Among these compared methods, DHSIS is the closest one to ours, but it is different in that it learnt deep priors from the single image fused from two observed images. Note that all competing methods set the regularization parameter fixed for all tested images.

For quality comparison, we take the scaling factor $s =$

TABLE II

AVERAGE RMSE, PSNR, ERGAS, SAM OF DIFFERENT METHODS WITH THREE SCALING FACTORS ($s = 8, 16$ AND 32) ON THE HARVARD DATASET.

	Metric	CSU	NSSR	DHSIS	CMS	proposed
$s = 8$	RMSE	1.91 ± 1.61	1.67 ± 1.42	1.80 ± 1.49	1.65 ± 1.47	1.61 ± 1.40
	PSNR	45.10 ± 4.73	46.29 ± 4.84	45.63 ± 4.78	46.49 ± 4.93	46.67 ± 4.83
	ERGAS	1.423 ± 0.914	1.219 ± 0.706	1.415 ± 0.748	1.355 ± 0.709	1.136 ± 0.676
	SAM	3.65 ± 1.39	3.46 ± 1.27	3.69 ± 1.39	3.57 ± 1.31	3.38 ± 1.29
$s = 16$	RMSE	2.01 ± 1.63	1.78 ± 1.57	1.80 ± 1.64	1.76 ± 1.59	1.73 ± 1.58
	PSNR	44.59 ± 4.58	45.95 ± 4.96	45.88 ± 4.99	46.06 ± 5.03	46.23 ± 4.98
	ERGAS	0.739 ± 0.461	0.653 ± 0.381	0.654 ± 0.403	0.721 ± 0.380	0.608 ± 0.377
	SAM	3.73 ± 1.41	3.58 ± 1.34	3.61 ± 1.38	3.68 ± 1.34	3.52 ± 1.36
$s = 32$	RMSE	2.14 ± 1.62	1.87 ± 1.64	1.92 ± 1.65	1.83 ± 1.63	1.83 ± 1.64
	PSNR	43.91 ± 4.42	45.54 ± 4.93	45.41 ± 4.90	45.79 ± 5.01	45.88 ± 4.97
	ERGAS	0.394 ± 0.240	0.363 ± 0.205	0.339 ± 0.205	0.381 ± 0.202	0.318 ± 0.199
	SAM	3.80 ± 1.42	3.73 ± 1.41	3.81 ± 1.46	3.76 ± 1.36	3.65 ± 1.42

TABLE III

AVERAGE RMSE, PSNR, ERGAS, SAM OF DIFFERENT METHODS WITH THE SCALING FACTOR $s = 8$ (GAUSSIAN BLUR KERNEL) ON THE CAVE DATASET AND THE HARVARD DATASET.

	Metric	CSU	NSSR	DHSIS	CMS	proposed
CAVE	RMSE	2.55 ± 0.97	1.88 ± 0.69	1.36 ± 0.45	1.57 ± 0.56	1.18 ± 0.39
	PSNR	41.85 ± 3.27	43.82 ± 3.11	46.95 ± 3.20	45.88 ± 2.97	48.14 ± 3.16
	ERGAS	1.138 ± 0.511	0.838 ± 0.362	0.619 ± 0.361	0.686 ± 0.300	0.540 ± 0.302
	SAM	6.43 ± 3.28	4.07 ± 1.51	3.75 ± 1.68	3.75 ± 1.42	3.26 ± 1.37
Harvard	RMSE	1.91 ± 1.62	1.85 ± 1.40	1.70 ± 1.55	1.63 ± 1.45	1.59 ± 1.38
	PSNR	45.07 ± 4.77	45.29 ± 4.66	46.29 ± 4.97	46.64 ± 4.97	46.71 ± 4.80
	ERGAS	1.420 ± 0.892	1.275 ± 0.703	1.228 ± 0.747	1.306 ± 0.698	1.130 ± 0.666
	SAM	3.72 ± 1.43	3.50 ± 1.29	3.45 ± 1.31	3.54 ± 1.31	3.37 ± 1.28

16 for example. Fig. 6 illustrates the reconstructed images and corresponding error maps of the test image *Real and fake pepper* at 550 nm and 690 nm bands, respectively. Visually, our method provides the best results in recovering the details of the latent HR HSIs and the corresponding error maps are closer to zero. Fig. 8 (a)-(c) shows that the spectral differences with the ground truth at three randomly selected points on the image *Real and fake peppers*. It can be observed that the proposed method gives the best approximation of the spectral curves in the latent HR HSIs. This demonstrates the efficacy of our method in recovering both the spatial and spectral information of the latent HR HSIs.

We evaluate the response curves with the scaling factor $s = 8$ on the CAVE dataset and search their optimal points under MDC. For each response curve, the hyperparameter μ is sampled on a 50 common logarithmic scale varying from 10^{-6} to 1. Fig. 7 shows the response curves and the points with the optimal parameter values. Note that these points may visually seem not optimal because we apply a much stronger zoom on the horizontal axis compared to the vertical one. The optimal parameter values corresponding to different images with different scaling factors are slightly different but unique in our case.

2) *Evaluation on Harvard Dataset:* We further evaluate the proposed method on the Harvard dataset. Different from the

CAVE dataset, the spatial size of images from the Harvard dataset is larger and slightly moving objects are not correctly aligned in the neighboring bands. As illustrated in Table II, with the same experimental setups as discussed above, the numerical results of the proposed method surpass other competing methods in most cases. Fig. 9 displays the reconstructed images and corresponding error maps of image *imgfl* at 650 nm band and 700 nm band with $s = 16$. It can be seen that our proposed method reconstructs more details of images and consequently produces smaller reconstruction error. As shown in Fig. 8 (d)-(f), spectral differences ($s = 16$) with the ground truth at three randomly selected points on the image *imgfl* clearly demonstrate that the proposed method performs best in estimating the spectral patterns of the latent HR HSIs.

3) *Evaluation with Optics Blur:* In the above experiments, we apply the uniform blurring matrix \mathbf{B} of size $s \times s$ to each band of the ground truth \mathbf{X} before the down-sampling operator. In the real-world hyperspectral imaging system, however, the optics blur may exist and it can be modeled by a Gaussian blurring kernel. To demonstrate the advantage of the proposed method when optics kernel occurs, we also simulate the LR HSI \mathbf{Y} by first applying 8×8 Gaussian kernel with standard deviation 3 to the latent HR HSI \mathbf{X} before down-sampling in both the vertical and horizontal directions with scaling factor 8. The numerical results on both the CAVE and Harvard datasets are reported in Table III. We observe that the proposed method

TABLE IV
AVERAGE RMSE, PSNR, ERGAS, SAM OF SOME COMPARED METHODS WITH THE SCALING FACTOR $s = 8$ (GAUSSIAN BLUR KERNEL) ON THE CAVE DATASET AND THE HARVARD DATASET.

Method	CAVE				Harvard			
	RMSE	PSNR	ERGAS	SAM	RMSE	PSNR	ERGAS	SAM
Bicubic	9.63	29.42	4.220	6.67	6.19	35.10	3.586	4.49
TSFN	1.43	46.39	0.637	3.76	1.71	46.22	1.175	3.47
Proposed without TSFN	1.69	45.36	0.766	4.11	1.33	47.03	1.546	3.95
Proposed with TSFN	1.18	48.14	0.540	3.26	1.61	46.64	1.132	3.41

outperforms other considered methods. This demonstrates the applicability of our method in real-world scenarios.

further enhance the applicability of our proposed method in real-world scenarios.

E. Ablation Study

As stated in Section III, we propose to learn the priors of the latent HR HSI via TSFN rather than using handcrafted regularizers. Here, we illustrate the effectiveness of TSFN, as well as its important role in our HSI super-resolution framework. First, we compare the up-sampled images \mathbf{Y}_{up} with the bicubic interpretation and $\tilde{\mathbf{X}}$, the outputs of our proposed TSFN. In addition, we evaluate the results of the proposed HSI super-resolution framework without TSFN. More specifically, we use the up-sampled images \mathbf{Y}_{up} as the approximation of the latent HR HSI, and then compared with our complete framework with TSFN. We conduct all these experiments on both the CAVE dataset and the Harvard dataset with Gaussian blur kernel mentioned above.

As shown in Table IV, the results of TSFN have significantly better quantitative performance compared with those of the bicubic interpretation. This illustrates the effectiveness of the priors representation of our method learnt via TSFN. Moreover, the performance of the proposed framework with TSFN exceeds that of the framework without TSFN, thus demonstrating TSFN is an indispensable part of our proposed HSI super-resolution method.

V. CONCLUSION

In this paper, we presented a deep priors-based HSI super-resolution method. Instead of using handcrafted image prior structures, we utilized the spatial-spectral priors learnt by the proposed TSFN. The output of TSFN was plugged into the regularizer to regularize the ill-posed problem. In addition, the regularization parameter was automatically estimated by adopting MDC on the response curve of the hyperspectral super-resolution problem with a golden-section search approach. Experimental results on two public datasets demonstrated that our proposed method can effectively handle scenarios with various scaling factor and blurring kernel setups.

In future works, the proposed HSI super-resolution method will be extended in two directions. On the one hand, to deal with larger scenes, e.g., in remote sensing imagery, an efficient fusion neural network with fewer parameters is designed to learn deep priors. On the other hand, to speed up hyperparameter tuning, a faster regularization parameter searching algorithm will be investigated. These attempts may

REFERENCES

- [1] J. M. Bioucas-Dias, A. Plaza, G. Camps-Valls, P. Scheunders, N. Nasrabadi, and J. Chanussot, "Hyperspectral remote sensing data analysis and future challenges," *IEEE Geosci. Remote Sens. Mag.*, vol. 1, no. 2, pp. 6–36, 2013.
- [2] H. Van Nguyen, A. Banerjee, and R. Chellappa, "Tracking via object reflectance using a hyperspectral video camera," in *Proc. IEEE Conf. Comput. Vis. Pattern Recognit. -Workshops. (CVPRW)*. IEEE, 2010, pp. 44–51.
- [3] Y. Tarabalka, J. Chanussot, and J. A. Benediktsson, "Segmentation and classification of hyperspectral images using watershed transformation," *Pattern Recognit.*, vol. 43, no. 7, pp. 2367–2379, 2010.
- [4] M. Fauvel, Y. Tarabalka, J. A. Benediktsson, J. Chanussot, and J. C. Tilton, "Advances in spectral-spatial classification of hyperspectral images," *Proc. IEEE*, vol. 101, no. 3, pp. 652–675, 2012.
- [5] C. Lanaras, E. Baltsavias, and K. Schindler, "Hyperspectral super-resolution by coupled spectral unmixing," in *Proc. IEEE Int. Conf. Comput. Vis. (ICCV)*, 2015, pp. 3586–3594.
- [6] L. Alparone, L. Wald, J. Chanussot, C. Thomas, P. Gamba, and L. M. Bruce, "Comparison of pansharpening algorithms: Outcome of the 2006 grs-s data-fusion contest," *IEEE Trans. Geosci. Remote Sens.*, vol. 45, no. 10, pp. 3012–3021, 2007.
- [7] N. Yokoya, C. Grohnfeldt, and J. Chanussot, "Hyperspectral and multispectral data fusion: A comparative review of the recent literature," *IEEE Geosci. Remote Sens. Mag.*, vol. 5, no. 2, pp. 29–56, 2017.
- [8] W. Carper, T. Lillesand, and R. Kiefer, "The use of intensity-hue-saturation transformations for merging spot panchromatic and multispectral image data," *Photogramm. Eng. Remote Sens.*, vol. 56, no. 4, pp. 459–467, 1990.
- [9] P. Kwarteng and A. Chavez, "Extracting spectral contrast in landsat thematic mapper image data using selective principal component analysis," *Photogramm. Eng. Remote Sens.*, vol. 55, no. 339–348, p. 1, 1989.
- [10] V. K. Shettigara, "A generalized component substitution technique for spatial enhancement of multispectral images using a higher resolution data set," *Photogramm. Eng. Remote Sens.*, vol. 58, no. 5, pp. 561–567, 1992.
- [11] J. Nunez, X. Otazu, O. Fors, A. Prades, V. Pala, and R. Arbiol, "Multiresolution-based image fusion with additive wavelet decomposition," *IEEE Trans. Geosci. Remote Sens.*, vol. 37, no. 3, pp. 1204–1211, 1999.
- [12] L. Zhang, W. Wei, C. Bai, Y. Gao, and Y. Zhang, "Exploiting clustering manifold structure for hyperspectral imagery super-resolution," *IEEE Trans. Image Process.*, vol. 27, no. 12, pp. 5969–5982, 2018.
- [13] N. Yokoya, T. Yairi, and A. Iwasaki, "Coupled nonnegative matrix factorization unmixing for hyperspectral and multispectral data fusion," *IEEE Trans. Geosci. Remote Sens.*, vol. 50, no. 2, pp. 528–537, 2011.
- [14] Q. Wei, J. Bioucas-Dias, N. Dobigeon, J.-Y. Tourneret, M. Chen, and S. Godsill, "Multiband image fusion based on spectral unmixing," *IEEE Trans. Geosci. Remote Sens.*, vol. 54, no. 12, pp. 7236–7249, 2016.
- [15] B. Huang, H. Song, H. Cui, J. Peng, and Z. Xu, "Spatial and spectral image fusion using sparse matrix factorization," *IEEE Trans. Geosci. Remote Sens.*, vol. 52, no. 3, pp. 1693–1704, 2013.
- [16] N. Akhtar, F. Shafait, and A. Mian, "Sparse spatio-spectral representation for hyperspectral image super-resolution," in *Proc. Eur. Conf. Comput. Vis. (ECCV)*. Springer, 2014, pp. 63–78.

- [17] Q. Wei, J. Bioucas-Dias, N. Dobigeon, and J.-Y. Tourneret, "Hyperspectral and multispectral image fusion based on a sparse representation," *IEEE Trans. Geosci. Remote Sens.*, vol. 53, no. 7, pp. 3658–3668, 2015.
- [18] W. Dong, F. Fu, G. Shi, X. Cao, J. Wu, G. Li, and X. Li, "Hyperspectral image super-resolution via non-negative structured sparse representation," *IEEE Trans. Image Process.*, vol. 25, no. 5, pp. 2337–2352, 2016.
- [19] S. Boyd, N. Parikh, E. Chu, B. Peleato, J. Eckstein *et al.*, "Distributed optimization and statistical learning via the alternating direction method of multipliers," *Found. Trends Mach. Learn.*, vol. 3, no. 1, pp. 1–122, 2011.
- [20] W. Yang, X. Zhang, Y. Tian, W. Wang, J.-H. Xue, and Q. Liao, "Deep learning for single image super-resolution: A brief review," *IEEE Trans. Multimedia.*, vol. 21, no. 12, pp. 3106–3121, 2019.
- [21] F. Palsson, J. R. Sveinsson, and M. O. Ulfarsson, "Multispectral and hyperspectral image fusion using a 3-d-convolutional neural network," *IEEE Geosci. Remote Sens. Lett.*, vol. 14, no. 5, pp. 639–643, 2017.
- [22] J. Yang, X. Fu, Y. Hu, Y. Huang, X. Ding, and J. Paisley, "Pannet: A deep network architecture for pan-sharpening," in *Proc. IEEE Int. Conf. Comput. Vis. (ICCV)*, 2017, pp. 5449–5457.
- [23] G. Scarpa, S. Vitale, and D. Cozzolino, "Target-adaptive cnn-based pansharpening," *IEEE Trans. Geosci. Remote Sens.*, vol. 56, no. 9, pp. 5443–5457, 2018.
- [24] Y. Li, J.-B. Huang, N. Ahuja, and M.-H. Yang, "Joint image filtering with deep convolutional networks," *IEEE Trans. Pattern Anal. Mach. Intell.*, vol. 41, no. 8, pp. 1909–1923, 2019.
- [25] X. Deng and P. L. Dragotti, "Deep convolutional neural network for multi-modal image restoration and fusion," *IEEE Trans. Pattern Anal. Mach. Intell.*, 2020.
- [26] Z. Shi, C. Chen, Z. Xiong, D. Liu, Z.-J. Zha, and F. Wu, "Deep residual attention network for spectral image super-resolution," in *Proceedings of the European Conference on Computer Vision (ECCV)*, 2018, pp. 0–0.
- [27] R. Dian, S. Li, A. Guo, and L. Fang, "Deep hyperspectral image sharpening," *IEEE Trans. Neural Netw. Learn. Syst.*, no. 99, pp. 1–11, 2018.
- [28] W. Xie, J. Lei, Y. Cui, Y. Li, and Q. Du, "Hyperspectral pansharpening with deep priors," *IEEE Trans. Neural Netw. Learn. Syst.*, 2019.
- [29] R. H. Bartels and G. W. Stewart, "Solution of the matrix equation $ax + xb = c$ [f4]," *Commun. ACM.*, vol. 15, no. 9, pp. 820–826, 1972.
- [30] G. H. Golub, M. Heath, and G. Wahba, "Generalized cross-validation as a method for choosing a good ridge parameter," *Technometrics*, vol. 21, no. 2, pp. 215–223, 1979.
- [31] N. P. Galatsanos and A. K. Katsaggelos, "Methods for choosing the regularization parameter and estimating the noise variance in image restoration and their relation," *IEEE Trans. Image Process.*, vol. 1, no. 3, pp. 322–336, 1992.
- [32] P. C. Hansen, "Analysis of discrete ill-posed problems by means of the l-curve," *SIAM Rev.*, vol. 34, no. 4, pp. 561–580, 1992.
- [33] L. Kaufman and A. Neumaier, "Regularization of ill-posed problems by envelope guided conjugate gradients," *J. Comput. Graph. Statist.*, vol. 6, no. 4, pp. 451–463, 1997.
- [34] K. Deb, *Multi-objective optimization using evolutionary algorithms*. John Wiley & Sons, 2001, vol. 16.
- [35] E. Van Den Berg and M. P. Friedlander, "Probing the pareto frontier for basis pursuit solutions," *SIAM J. Sci. Comput.*, vol. 31, no. 2, pp. 890–912, 2009.
- [36] Y. Song, D. Brie, E.-H. Djermoune, and S. Henrot, "Regularization parameter estimation for non-negative hyperspectral image deconvolution," *IEEE Trans. Image Process.*, vol. 25, no. 11, pp. 5316–5330, 2016.
- [37] S. Sreehari, S. V. Venkatakrishnan, B. Wohlberg, G. T. Buzzard, L. F. Drummy, J. P. Simmons, and C. A. Bouman, "Plug-and-play priors for bright field electron tomography and sparse interpolation," *IEEE Trans. Comput. Imaging*, vol. 2, no. 4, pp. 408–423, 2016.
- [38] A. Teodoro, J. Bioucas-Dias, and M. Figueiredo, "A convergent image fusion algorithm using scene-adapted gaussian-mixture-based denoising," *IEEE Trans. Image Process.*, vol. 28, no. 1, pp. 451–463, 2018.
- [39] X. Wang, J. Chen, C. Richard, and D. Brie, "Learning spectral-spatial prior via 3DDnCNN for hyperspectral image deconvolution," in *IEEE Int. Conf. on Acoust. Speech, Signal Process (ICASSP)*. IEEE, 2020, pp. 2403–2407.
- [40] K. Simonyan and A. Zisserman, "Two-stream convolutional networks for action recognition in videos," in *Proc. Adv. Neural Inf. Process. Syst. (NeurIPS)*, 2014, pp. 568–576.
- [41] C. Feichtenhofer, A. Pinz, and A. Zisserman, "Convolutional two-stream network fusion for video action recognition," in *Proc. IEEE Conf. Comput. Vis. Pattern Recognit. (CVPR)*, 2016, pp. 1933–1941.
- [42] X. Xu, W. Li, Q. Ran, Q. Du, L. Gao, and B. Zhang, "Multisource remote sensing data classification based on convolutional neural network," *IEEE Trans. Geosci. Remote Sens.*, vol. 56, no. 2, pp. 937–949, 2017.
- [43] K. He, X. Zhang, S. Ren, and J. Sun, "Deep residual learning for image recognition," in *Proc. IEEE Conf. Comput. Vis. Pattern Recognit. (CVPR)*, 2016, pp. 770–778.
- [44] —, "Identity mappings in deep residual networks," in *Proc. Eur. Conf. Comput. Vis. (ECCV)*. Springer, 2016, pp. 630–645.
- [45] J. Kim, J. Kwon Lee, and K. Mu Lee, "Deeply-recursive convolutional network for image super-resolution," in *Proc. IEEE Conf. Comput. Vis. Pattern Recognit. (CVPR)*, 2016, pp. 1637–1645.
- [46] C. Ledig, L. Theis, F. Huszar, J. Caballero, A. Cunningham, A. Acosta, A. Aitken, A. Tejani, J. Totz, Z. Wang *et al.*, "Photo-realistic single image super-resolution using a generative adversarial network," in *Proc. IEEE Conf. Comput. Vis. Pattern Recognit. (CVPR)*, 2017, pp. 4681–4690.
- [47] S. Ioffe and C. Szegedy, "Batch normalization: Accelerating deep network training by reducing internal covariate shift," *arXiv preprint arXiv:1502.03167*, 2015.
- [48] K. He, X. Zhang, S. Ren, and J. Sun, "Delving deep into rectifiers: Surpassing human-level performance on imagenet classification," in *Proc. IEEE Int. Conf. Comput. Vis. (ICCV)*, 2015, pp. 1026–1034.
- [49] Q. Wei, N. Dobigeon, and J.-Y. Tourneret, "Fast fusion of multi-band images based on solving a sylvester equation," *IEEE Trans. Image Process.*, vol. 24, no. 11, pp. 4109–4121, 2015.
- [50] F. Yasuma, T. Mitsunaga, D. Iso, and S. K. Nayar, "Generalized assorted pixel camera: postcapture control of resolution, dynamic range, and spectrum," *IEEE Trans. Image Process.*, vol. 19, no. 9, pp. 2241–2253, 2010.
- [51] A. Chakrabarti and T. Zickler, "Statistics of real-world hyperspectral images," in *Proc. IEEE Conf. Comput. Vis. Pattern Recognit. (CVPR)*, 2011, pp. 193–200.
- [52] J. Kim, "Iterated grid search algorithm on unimodal criteria," Ph.D. dissertation, Virginia Tech, 1997.
- [53] D. P. Kingma and J. Ba, "Adam: A method for stochastic optimization," *arXiv preprint arXiv:1412.6980*, 2014.
- [54] L. Wald, "Quality of high resolution synthesised images: Is there a simple criterion?" 2000.
- [55] R. H. Yuhas, A. F. Goetz, and J. W. Boardman, "Discrimination among semi-arid landscape endmembers using the spectral angle mapper (sam) algorithm," 1992.